

Role of proppant distribution on the evolution of hydraulic fracture conductivity

Jiehao Wang^{*}, Derek Elsworth

Department of Energy and Mineral Engineering, EMS Energy Institute and G3 Center, Pennsylvania State University, University Park, PA 16802, USA



ARTICLE INFO

Keywords:

Hydraulic fracturing
Proppant distribution
Residual opening
Proppant embedment
Fracture conductivity
Channel fracturing

ABSTRACT

The residual opening of fluid-driven fractures is conditioned by proppant distribution and has a significant impact on fracture conductivity - a key parameter to determine fluid production rate and well performance. A 2D model follows the evolution of the residual aperture profile and conductivity of fractures partially/fully filled with proppant packs. The model accommodates the mechanical response of proppant packs in response to closure of arbitrarily rough fractures and the evolution of proppant embedment. The numerical model is validated against existing models and an analytic solution. Proppant may accumulate in a bank at the fracture base during slick water fracturing, and as hydraulic pressure is released, an arched zone forms at the top of the proppant bank as a result of partial closure of the overlaying unpropped fracture. The width and height of the arched zone decreases as the fluid pressure declines, and is further reduced where low concentrations of proppant fill the fracture or where the formation is highly compressible. This high-conductivity arch represents a preferential flow channel and significantly influences the distribution of fluid transport and overall fracture transmissivity. However, elevated compacting stresses and evolving proppant embedment at the top of the settled proppant bed reduce the aperture and diminish the effectiveness of this highly-conductive zone, with time. Two-dimensional analyses are performed on the fractures created by channel fracturing, showing that the open channels formed between proppant pillars dramatically improve fracture transmissivity if they are maintained throughout the lifetime of the fracture. However, for a fixed proppant pillar height, a large proppant pillar spacing results in the premature closure of the flow channels, while a small spacing narrows the existing channels. Such a model provides a rational means to design optimal distribution of the proppant pillars using deformation moduli of the host to control pillar deformation and flexural spans of the fracture wall.

1. Introduction

Hydraulic fracturing is widely used for well completions to enhance hydrocarbon recovery. High-pressure fluid is injected into the well to initiate and propagate a fluid-driven fracture. At some stage, proppant is added to the fracturing fluid and the proppant-laden mixture inflates, drives and then fills the fractures. Once pumping is stopped, fluid pressure decreases and the fractures close under in-situ stresses, trapping the proppant between the fracture walls. The proppant “props-open” the fracture to improve fracture conductivity and retain this conductivity as effective stresses build and compact the proppant pack.

A variety of approaches have been developed to represent the mechanisms of hydraulic fracturing as a coupled problem of solid mechanics (fracture initiation, propagation and inflation) and fluid mechanics (fluid flow within fractures and leak-off into formations). The

solid mechanics aspects of hydraulic fracturing has been comprehensively reviewed by Adachi et al. (2007), Rahman and Rahman (2010), and Detournay (2016), among others, while reviews of the fluid mechanics aspects can be found in Osipov (2017). Proppant transport and placement within hydraulic fractures are controlled by fracture geometry, the rheology of the fracturing fluids, pumping schedule, and proppant particle shape, size and density. Extensive work has explored the complex interactive processes involved in proppant transport and placement, including those by Kern et al. (1959), Daneshy (1978), Ouyang et al. (1997) and Dontsov and Peirce (2015).

Conventional fracturing fluids, typified by linear or crosslinked gels, have high viscosities that enable injected proppant to remain suspended over extended periods and result in uniform proppant packs (Economides and Nolte, 2000). Conversely, low viscosity fluids, including common slick water fracturing (Palisch et al., 2010), result in the proppant settling

^{*} Corresponding author.

E-mail addresses: jiehao.wang@psu.edu (J. Wang), elsworth@psu.edu (D. Elsworth).

from suspension and accumulating in an immobile proppant bed (Wang et al., 2003) (Fig. 1). The proppant distribution within the fracture ultimately determines the closure behavior of the fracture, and this in turn has a significant influence on fracture conductivity - a key parameter controlling well performance. Fractures with a basal proppant bank exhibit a complex post-closure geometry due to the differential closure of the propped and unpropped portions (Cleary, 1980). Simple models (McLennan et al., 2008; Warpinski, 2010) show the formation of a high-conductivity arch at the top of the proppant bank. The presence and impact of this high-conductivity arch is generally ignored in most models (Gu and Mohanty, 2014; Shiozawa and McClure, 2016), but is considered by some (Cipolla et al., 2009; Liu et al., 2017), suggesting that it may significantly affect well performance. Recent studies explore the residual opening of fractures partially filled with proppant packs (Neto and Kotousov, 2013a; 2013b; Neto et al., 2015; and Khanna et al., 2014), accommodating KGD type fractures where the proppant pack is distributed symmetrically about the wellbore (fracture center). Such semi-analytical approaches define fracture residual opening based on the Distributed Dislocation Technique. These studies confirm the significant impact of proppant distribution and its mechanical properties on the residual fracture profiles and well performance.

Such models typically only consider specific proppant distributions, assuming complete settling (Warpinski, 2010) or uniform distribution symmetric about the fracture center (Neto and Kotousov, 2013a, 2013b; Neto et al., 2015; Khanna et al., 2014). However, proppant placement within the fracture can be complex and heterogeneous, as modulated by the roughness and tortuosity of fracture (Vincent, 2012), or as a result of some unconventional methods of proppant injection such as periodic injection (Tinsley and Williams, 1975) or channel fracturing (D'Huteau et al., 2011). In this study, a non-local model of residual opening is developed based on 2D elasticity using integral equations where the proppant pack is allowed to have arbitrary distribution and concentration. The proposed model is capable of accommodating the mechanical response of proppant packs including the influence of fracture closure on rough surfaces, and proppant embedment into fracture walls - enabling the evaluation of fracture conductivity after ultimate fracture closure. The model is developed, validated and exercised in parametric studies, in the following and it is utilized to analyze residual aperture profiles and conductivities with several different proppant distributions.

2. Mathematical formulation

The PKN approximation can be applied for a blade-shaped fracture penetrating an isotropic, homogenous and linearly elastic formation (Nordgren, 1972; Perkins and Kern, 1961), as illustrated in Fig. 1. The

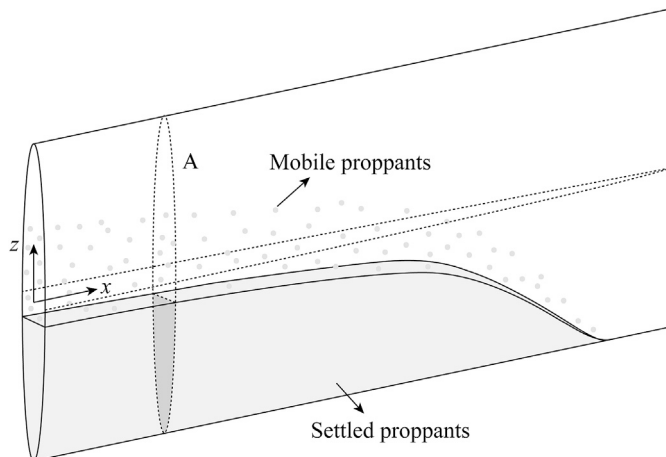


Fig. 1. Schematic of proppant transport and placement for slick water fracturing. (Cross section A is shown in detail in Fig. 2).

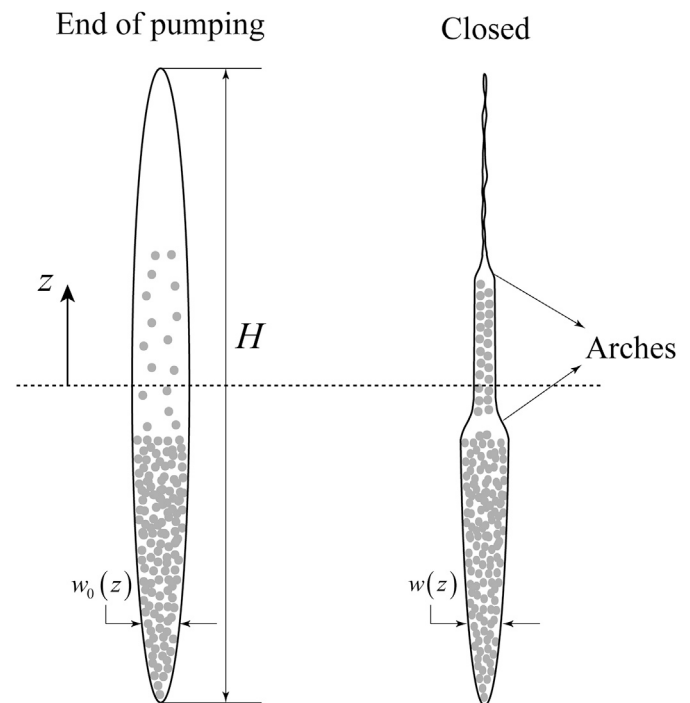


Fig. 2. Cross section of a blade-shaped fracture partially filled with proppant at the end of pumping (left) and after fracture closure (right).

geometry of the fracture cross section (Fig. 2) may accommodate varied proppant distributions at the conclusion of pumping. The cross-section of the elastic fracture is an ellipse of height H and width $w_0(z)$, and may be only partially filled with proppant. This distribution results from proppant settling or capture and plugging between the rough fracture walls, defining a proppant volumetric concentration $c_0(z)$ that varies in the z -direction. At the conclusion of the treatment, when pumping stops, leak-off of the residual fracturing fluid into the surrounding formation allows the fracture walls to close and to compact the proppant pack. Compaction of the pack will also be accompanied by proppant embedment into the fracture faces and flexural displacement of the unsupported spans of the fracture - leaving residual apertures absent proppant (Warpinski, 2010) (Fig. 2). Note that, although a case with most of the proppant settled to the bottom is shown in Fig. 2, this proposed model is applicable for any arbitrary proppant distribution, including the case of uniform proppant distribution within the fracture and the case where several isolated proppant banks are formed over the fracture height due to tortuous fracture walls or channel fracturing.

2.1. Elastic integral equations

Upon the closure of the fracture, ensemble stress applied on the fracture walls, $\sigma_n(z)$, is superposed by far-field stress, $\sigma_h(z)$, fluid pressure within the fracture, $p(z)$, back stress from the proppant pack, $\sigma_p(z)$, and back stress from the fracture asperities, $\sigma_a(z)$, as,

$$\sigma_n(z) = p(z) + \sigma_p(z) + \sigma_a(z) - \sigma_h(z). \quad (1)$$

For a linear elastic system, the residual opening profile, $w(z)$, and the ensemble stress applied on the fracture walls in plane strain, $\sigma_n(z)$, can be described by an integral equation

$$w(z) = \frac{4}{\pi E'} \int_{-H/2}^{H/2} \sigma_n(s) G(z, s) ds - 2w_e(z), \quad (2)$$

where $E' = E/(1 - \nu^2)$ is the plane strain Young's modulus, $w_e(z)$ is the depth of proppant embedment (the factor 2 accounts for the embedment into both walls of the fracture) and $G(z, s)$ is a singular elastic kernel

(Tada et al., 2000),

$$G(z, s) = \cosh^{-1} \frac{H^2 - 4sz}{2H|z - s|}, \quad (3)$$

describing the fracture aperture at z due to a pair of unit forces applied on the fracture faces at s . This kernel describes the non-local effect of the local ensemble normal stress across the height of the fracture. Note that the integral in Eq. (2) has to be understood in the sense of a Cauchy principal value.

2.2. Compaction of proppant pack

This study is focused on the fracture closure process, beginning when the pumping stops. The conditions at the end of the pumping define the initial conditions for this analysis. A number of numerical studies have been conducted to simulate proppant transport and placement in terms of proppant volumetric concentration (Dontsov and Peirce, 2015; Shiozawa and McClure, 2016; Wang and Elsworth, 2017). Thus, in this analysis, it is convenient to define the proppant distribution using the distribution of proppant volumetric concentration. The initial proppant volumetric concentration is defined as the ratio of proppant volume, $V_p(z)$, to initial fracture volume, $V_f(z)$, $c_0(z) = V_p(z)/V_f(z)$. The maximum value of the initial proppant concentration, c_{max} , is dependent on the proppant particle shape and their packing arrangement. This is always less than unity due to the presence of void spaces. For convenience, a normalized initial proppant concentration is introduced as $\bar{c}_0(z) = c_0(z)/c_{max}$, with $0 \leq \bar{c}_0(z) \leq 1$. Therefore, the initial width of the proppant pack can be defined as

$$w_{p0}(z) = w_0(z)\bar{c}_0(z), \quad (4)$$

where $w_0(z)$ is the initial fracture width. It is assumed that the proppant pack is a granular assembly comprising uniform, rigid spheres, and that the deformation of the proppant pack results from changes in pore volume. Compressibility of the proppant packs is defined as

$$c_p = -\frac{1}{w_p(z)} \frac{\partial w_p(z)}{\partial \sigma_p(z)}, \quad (5)$$

where $w_p(z) < w_{p0}(z)$ is the width of the compacting proppant pack, congruent with the fracture width. To simplify the problem, the compressibility of the proppant pack is assumed to be constant. Integrating Eq. (5) yields the compacting stress applied on the proppant pack when the equilibrium state is reached as (Shiozawa and McClure, 2016),

$$\sigma_p(z) = \begin{cases} \frac{1}{c_p} \ln \frac{w_{p0}(z)}{w(z)}, & w(z) < w_{p0}(z) \\ 0, & w(z) \geq w_{p0}(z) \end{cases}, \quad (6)$$

providing a linearized dependence of the compacting stress, $\sigma_p(z)$, on the logarithm of the deformation ratio, $w_{p0}(z)/w(z)$. More sophisticated compaction models can be used at the expense of additional empirical parameters or coefficients (Neto et al., 2015; Pestana and Whittle, 1995) and added computational complexity.

2.3. Mechanical response of rough fracture

Fractures in hydrocarbon and geothermal reservoirs are typically rough with asperities distributed across the surface area (van Dam et al., 2000; Wang and Sharma, 2017). The roughness of the fracture walls is neglected in Eq. (6) where it is small in contrast to its wavelength and the aperture of the fracture (Stoddard et al., 2011). However, the roughness of the fracture walls may be considered for the unpropped fracture segments, where roughness controls the closure of the two elastic surfaces in contact. Experimental observations have shown the non-linear nature of

the mechanical responses of rough discontinuities in rock (Zangerl et al., 2008; Brady and Brown, 2006), which can be described by the empirical Barton-Bandis fracture closure model (Bandis et al., 1983; Barton et al., 1985) as

$$\sigma_a(z) = \begin{cases} \frac{w_{a0} - w(z)}{b_1 - b_2[w_{a0} - w(z)]}, & w(z) < w_{a0} \\ 0, & w(z) \geq w_{a0} \end{cases}, \quad (7)$$

where $\sigma_a(z)$ is the contact stress applied on the fracture asperities, w_{a0} is the asperity width, i.e. the critical aperture at which fracture walls begin to contact, b_1 is a constant representing the compliance of the asperity, and $b_2 = b_1/w_{a0}$. Note that this model gives $\sigma_a(z) = 0$ at $w(z) = w_{a0}$ and an infinite $\sigma_a(z)$ as $w(z)$ goes to zero, implying that the fracture is not allowed to completely close.

2.4. Proppant embedment

After fracture closure, proppant particles may embed into the fracture walls resulting in the reduction of fracture width and conductivity (Alramahi and Sundberg, 2012; Lee et al., 2010; Wen et al., 2007). A proppant embedment model accommodates this effect. In this study, elastic Hertzian contact is applied to describe proppant embedment (Khanna et al., 2012; Chen et al., 2017).

Consider the classic Hertzian contact problem between a spherical indenter and an elastic semi-infinite half-space as shown in Fig. 3. The radius of the contact zone, a , can be evaluated as (Fischer-Cripps, 2007)

$$a^3 = \frac{3PR}{4E^*}, \quad (8)$$

where P is the indenter load, R is the indenter radius, and E^* is the combined modulus of the

Indenter and the half-space given by (Fischer-Cripps, 2007)

$$\frac{1}{E^*} = \frac{1 - \nu^2}{E} + \frac{1 - \nu_p^2}{E_p}, \quad (9)$$

where E_p and ν_p are the Young's modulus and Poisson's ratio for the indenter. When the indenter is much more rigid than the half-space, i.e. $E_p \gg E$, which is the general case for proppant embedment, Eq. (9) reduces to

$$E^* = \frac{E}{1 - \nu^2} = E'. \quad (10)$$

Combining Eqs. (8) and (10), the mean contact pressure, p_m , which is given by the indenter load divided by the projected contact area, can be written as

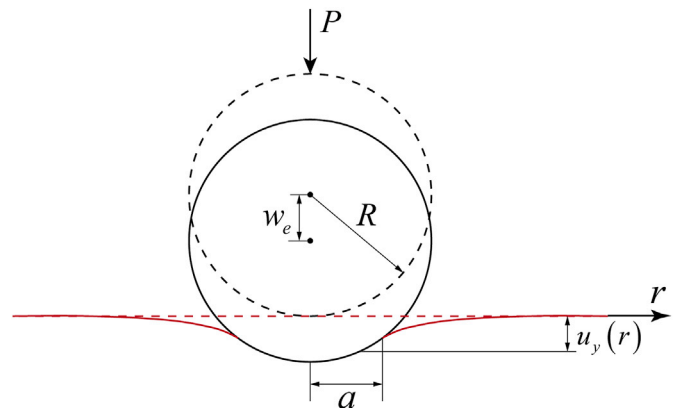


Fig. 3. Hertzian contact problem between a rigid sphere and an elastic semi-infinite half-space.

$$p_m = \frac{P}{\pi a^2} = \frac{4}{3} \frac{E'}{\pi} \frac{a}{R}. \quad (11)$$

The vertical normal displacement of the surface at a distance r from the centerline-symmetry point of contact can be calculated as (Fischer-Cripps, 2007)

$$u_y(r) = \begin{cases} \frac{3\pi}{8aE'}(2a^2 - r^2), & r \leq a \\ \frac{3}{4aE'} p_m \left[(2a^2 - r^2) \sin^{-1} \frac{a}{r} + ar \left(1 - \frac{a^2}{r^2} \right)^{1/2} \right], & r > a \end{cases}. \quad (12)$$

Eq. (12) has a maximum value when $r = 0$, which can be expressed by combining Eqs. (11) and (12) as

$$u_{y \max} = R \left(\frac{3\pi}{4E'} p_m \right)^2. \quad (13)$$

For the proppant pack, the mean contact pressure, $p_m(z)$, and the compacting stress, $\sigma_p(z)$, are related as

$$p_m(z) \pi a^2 = \sigma_p(z) \eta R^2, \quad (14)$$

where $\eta \geq 2\sqrt{3}$ is a constant determined by the proppant packing (see Appendix). Combining Eqs. (11) and (14), yields

$$p_m(z) = \left[\frac{16\eta E'^2}{9\pi^3} \sigma_p(z) \right]^{1/3}. \quad (15)$$

Therefore, incorporating Eqs. (6) and (15) into Eq. (13) gives the proppant embedment (the maximum vertical normal displacement $u_{y \max}$) as

$$w_e(z) = \begin{cases} R \left(\frac{3\pi}{4E'} \right)^2 \left[\frac{16\eta E'^2}{9\pi^3 c_p} \ln \frac{w_{p0}(z)}{w(z)} \right]^{2/3}, & w(z) < w_{p0}(z) \\ 0, & w(z) \geq w_{p0}(z) \end{cases}. \quad (16)$$

According to Eq. (16), the proppant embedment is proportional to the compacting stress to the power of 2/3, i.e. $w_e \sim \sigma_p^{2/3}$, which is consistent with experimental results (Alramahi and Sundberg, 2012) where the proppant embedment is observed as $w_e \sim \sigma_p^\lambda$ with λ in the range of 0.514–0.707 (Chen et al., 2017).

The final governing equation for the fracture residual opening, $w(z)$, is obtained by substituting Eqs. (1), (6), (7) and (16) into Eq. (2), where $W(z)$ is the only unknown. However, an analytical solution for the singular integral equation, Eq. (2), is difficult to obtain due to the strong non-linear behavior of the compaction of the proppant pack, asperity contact and proppant embedment. Thus, a numerical solution procedure is employed in this study, as discussed later in Section 4.

2.5. Fracture conductivity model

Hydraulic fracture conductivity is a key parameter in representing ultimate fluid transport in the reservoir (Economides and Nolte, 2000). The fracture conductivity is defined as the product of the fracture width and the permeability of the compacted proppant pack or the unpropried fracture.

According to the parallel plate model, the permeability of an unpropried fracture can be written as (Witherspoon et al., 1980; Zimmerman and Bodvarsson, 1996)

$$k_f(z) = \frac{w^2(z)}{12}. \quad (17)$$

Note that transmissivity of a PKN fracture without proppant is given by integrating the product of $k_f(z)$ and $w(z)$ over the fracture height. Dividing the fracture transmissivity by the area of fracture cross-section gives the averaged fracture permeability $\bar{k}_f = w_{\max}^2/16$, where w_{\max} is the

fracture width at $z = 0$ (Perkins and Kern, 1961; Nordgren, 1972).

For a compacted proppant pack, the permeability, $k_p(z)$, is related to the porosity, $\phi(z)$, which is defined as

$$\phi(z) = \frac{V_p(z)}{V_b(z)} = 1 - \frac{V_s(z)}{V_b(z)} = 1 - \frac{w_0(z) \bar{c}_0(z) c_{\max}}{w(z)}, \quad (18)$$

where $V_b(z)$ is the bulk volume of the proppant pack, $V_p(z)$ is the volume of the pore space within the proppant pack and $V_s(z)$ is the volume of the solid phase, i.e. the proppant particles. One of the well-known porosity-permeability relationships is the Kozeny-Carman model (Kozeny, 1927; Carman, 1937) expressed as

$$k_p(z) = \frac{1}{k_K S_{Vgr}^2} \frac{\phi^3(z)}{[1 - \phi(z)]^2}, \quad (19)$$

where k_K is the Kozeny-Carman constant and S_{Vgr} is the total particle surface area per unit volume of the solid phase. For packed beds with uniform spheres of radius R , generally we have $k_K = 5$ and $S_{Vgr} = (4\pi R^2)/(4\pi R^3/3) = 3/R$, reducing Eq. (19) to

$$k_p(z) = \frac{R^2}{45} \frac{\phi^3(z)}{[1 - \phi(z)]^2}. \quad (20)$$

If the initial proppant concentration $0 < c_0(z) < 1$, the proppant pack will not be compacted at the beginning of the fracture closure process until a sufficiently small fracture aperture is reached, i.e. $w(z) \leq w_{p0}(z)$. Such uncompacted proppant may also exist in the arched zones when the fracture has closed. Under those conditions, the permeability models for the unpropried fracture and compacted proppant pack [Eqs. (17) and (20)] might no longer be applicable. Considering a smoothly varying interpolation function, $\hat{Q}^s(\bar{c}, w/R)$, proposed by Dontsov and Peirce (2014) describing changes of slurry mobility with proppant concentration and fracture width, the permeability of a fracture containing uncompacted proppant can be written as

$$k'_f(z) = \frac{w^2(z)}{12} \hat{Q}^s\left(\bar{c}(z), \frac{w(z)}{R}\right), \quad (21)$$

where $\bar{c}(z) = \bar{c}_0(z) w_0(z)/w(z)$ is the proppant concentration during fracture closure and function \hat{Q}^s can be expressed as

$$\hat{Q}^s\left(\bar{c}, \frac{w}{R}\right) = Q^s(\bar{c}) + \frac{R^2}{w^2} \bar{c} \frac{8(1 - c_{\max})^{\bar{\alpha}}}{3c_{\max}}, \quad (22)$$

where $Q^s(\bar{c})$ is a function of \bar{c} only with $Q^s(0) = 1$ and $Q^s(1) = 0$ and is calculated numerically, and $\bar{\alpha} = 3 - \ln(10c_{\max})/\ln(1 - c_{\max})$. As an illustration, Fig. 4 plots the function \hat{Q}^s versus \bar{c} for different values of w/R . A detailed explanation of Eq. (22) can be found in Dontsov and Peirce (2014). Appropriately, Eq. (21) reduces to Eq. (17) when $\bar{c} = 0$ (unpropried fracture) and reduces to Eq. (20) when $\bar{c} = 1$ (proppant pack begins to be compacted, i.e. when $\phi = 1 - c_{\max}$).

Combining Eqs. (17), (20) and (21), yields

$$C(z) = \begin{cases} \frac{w^3(z)}{12} \hat{Q}^s\left(\bar{c}(z), \frac{w(z)}{R}\right), & w(z) \geq w_{p0}(z) \\ w(z) \frac{R^2}{45} \frac{\phi^3(z)}{[1 - \phi(z)]^2}, & w(z) < w_{p0}(z) \end{cases}, \quad (23)$$

which defines the conductivity of a fracture that is partially filled with proppant.

3. Numerical algorithm

As discussed previously, the strongly non-linear behavior due to compaction of the proppant pack, fracture closure, asperity contact and

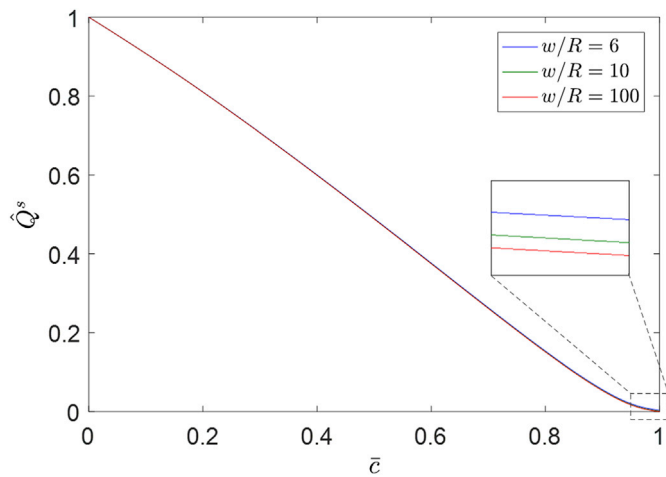


Fig. 4. The function \hat{Q}^s versus normalized proppant concentration \bar{c} for three specified values of w/R .

proppant embedment renders an exact analytical solution unavailable for the singular integral equation, Eq. (2). The displacement discontinuity method with constant strength elements (Crouch, 1976) is implemented in this study to solve Eq. (2) numerically.

The problem domain is discretized into N elements, as shown in Fig. 5, with each element consisting of a central collocation node, z_j , and two auxiliary integration nodes, s_i and s_{i+1} , located at the element ends, which are given, respectively, by

$$z_j = -\frac{(N+1)H}{2N} + \frac{H}{N}j, \quad j = 1, 2, \dots, N, \quad (24)$$

And

$$s_i = -\frac{(N+2)H}{2N} + \frac{H}{N}i, \quad i = 1, 2, \dots, N+1. \quad (25)$$

The elastic equation for width, Eq. (2), can be discretized as

$$F[w(z_j)] = w(z_j) - \frac{2}{\pi E'} \sum_{i=1}^{N+1} \{ (z_i - z_{i-1}) [\sigma_n(z_{i-1}) + \sigma_n(z_i)] G(z_j, s_i) \} + 2w_e(z_j) = 0, \quad j = 1, 2, \dots, N, \quad (26)$$

with $z_0 = -H/2$, $z_{N+1} = H/2$, $\sigma_n(z_0) = \sigma_n(z_1)$, and $\sigma_n(z_{N+1}) = \sigma_n(z_N)$. Following Eqs. (2), (6), (7) and (16), both the ensemble stress applied on the fracture walls at position z_j , $\sigma_n(z_j)$, and the proppant embedment at position z_j , $w_e(z_j)$ can be written as functions of $w(z_j)$. Therefore, the discretized form [Eq. (26)] represents a system of N non-linear algebraic equations in N unknowns $w(z_j)$, $j = 1, 2, \dots, N$, and can be solved using the Newton–Raphson iterative scheme. The matrix notion of the Newton–Raphson solution of Eq. (26) at the l th iteration takes the form

$$\mathbf{w}^{(l)} = \mathbf{w}^{(l-1)} - \mathbf{J}^{-1(l-1)} \mathbf{F}^{(l-1)}, \quad (27)$$

where the superscripts in parentheses (i.e., l and $l-1$) are the iteration steps, and the set of arrays are

$$\mathbf{w} = \{ w(z_1) \quad w(z_2) \quad \dots \quad w(z_N) \}^T, \quad (28)$$

$$\mathbf{F} = \{ F[w(z_1)] \quad F[w(z_2)] \quad \dots \quad F[w(z_N)] \}^T, \quad (29)$$

And

$$\mathbf{J} = \begin{Bmatrix} \frac{\partial F[w(z_1)]}{\partial w(z_1)} & \frac{\partial F[w(z_1)]}{\partial w(z_2)} & \dots & \frac{\partial F[w(z_1)]}{\partial w(z_N)} \\ \frac{\partial F[w(z_2)]}{\partial w(z_1)} & \frac{\partial F[w(z_2)]}{\partial w(z_2)} & \dots & \frac{\partial F[w(z_2)]}{\partial w(z_N)} \\ \vdots & \vdots & \ddots & \vdots \\ \frac{\partial F[w(z_N)]}{\partial w(z_1)} & \frac{\partial F[w(z_N)]}{\partial w(z_2)} & \dots & \frac{\partial F[w(z_N)]}{\partial w(z_N)} \end{Bmatrix}, \quad (30)$$

where the Jacobian for the system, \mathbf{J} , is evaluated using a finite difference approximation at each iteration. The iteration process, Eq. (27), is repeated until the convergence condition is met. After the fracture residual opening profile, $w(z)$, is obtained, the fracture conductivity, $C(z)$, can be evaluated according to Eq. (23).

4. Numerical results and discussions

A series of numerical simulations are completed with the fracture closure model proposed in this study. First, this model is comparing predictions against existing models and an analytic solution. Second, we perform numerical simulations, including a base case and a series of parametric studies, in which a proppant bank is deposited at the fracture base by slick water fracturing. Third, this model is utilized to analyze residual aperture profiles and conductivities of fractures resulting from channel fracturing.

4.1. Model validation

A semi-analytical method for calculating the residual opening of fractures partially filled with proppant has been developed by Neto and Kotousov (2013a). This is based on the Distributed Dislocation Technique and Terzaghi's classical consolidation model. This Neto-Kotousov model considers KGD type fractures where the plane strain condition is assumed in the direction of the fracture height, and where the proppant is distributed symmetrically about the fracture center, as shown in Fig. 6.

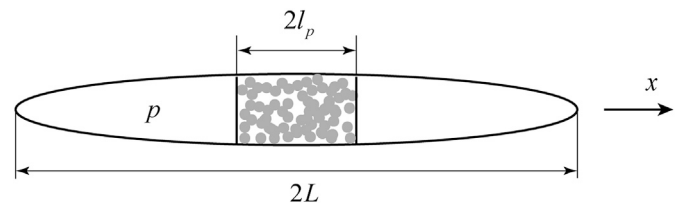


Fig. 6. Geometry of a KGD type fracture with proppant distributed symmetrically about the fracture center. (Origin is placed at the fracture center).

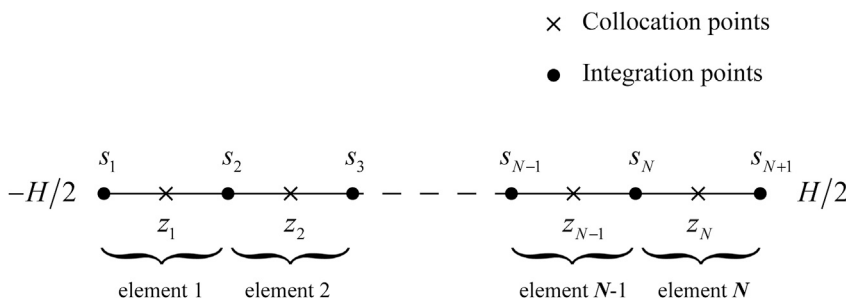


Fig. 5. Computational mesh used in this study.

Note that, although the established model in this study is primarily focused on a blade-like (PKN) fracture, where the plane strain condition is approximated in the direction of fracture length, it can also be straightforwardly applied to a KGD type fracture by replacing fracture height with fracture length in Eq. (2). With the parameters listed in Table 1, two cases with different lengths of the propped portion of the KGD type fracture, $2l_p = 2$ m and $2l_p = 6$ m, are considered here. The residual opening profiles are obtained using the proposed model and compared with the Neto-Kotousov model. Proppant embedment is ignored, i.e. $w_e(x) = 0$, to make the two models directly comparable. Taking advantage of the half symmetry of the problem geometry, the fracture residual opening profiles of half-length are shown in Fig. 7. It can be seen that the proposed model agrees with the Neto-Kotousov model very well. The slight differences may be due to the different models of proppant compaction that are used in the two models.

If the uniform internal fluid pressure is increased to $p \geq \sigma_h + \bar{w}_0 E' / (\pi L) = 14.77$ MPa, the fracture will dilate, pushing the fracture walls away from the proppant pack. This condition is equivalent to the well-known problem of a 2D static pressurized crack under a plane strain condition (Sneddon and Elliott, 1946), which takes the analytic solution for the fracture profile as

$$w(x) = \frac{4(p - \sigma_h)}{E'} \sqrt{L^2 - x^2}. \tag{31}$$

Further, considering an even higher pressure, $p = 18$ MPa, the fracture profile is calculated by the proposed model. As shown in Fig. 7, there is an excellent agreement between the proposed model and the analytic solution.

Table 1
Input parameters used for model validation.

Parameters	Values
Plane strain Young's modulus E'	25 GPa
Compressibility of proppant pack c_p	$3.9 \times 10^{-8} \text{ Pa}^{-1}$
Initial averaged fracture width \bar{w}_0	3 mm
Far-field stress σ_h	10 MPa
Internal fluid pressure p	10 MPa
Fracture half-length L	5 m
Initial proppant concentration $c_0(x \leq l_p)$	1
Initial proppant concentration $c_0(x > l_p)$	0
Asperity width w_a	0.1 mm

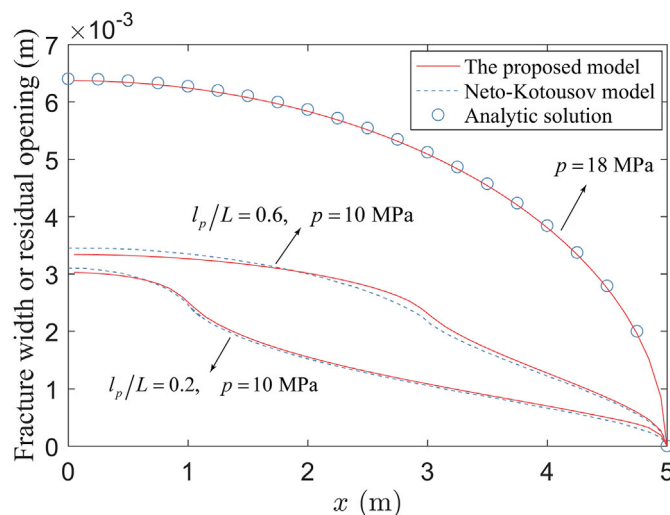


Fig. 7. Calculated residual openings of a KGD type fracture filled with different amount of proppant and under different fluid pressure. Only half-length of the fracture is shown here by taking advantage of the problem half symmetry. The results are compared with existing models (Neto and Kotousov, 2013a) and an analytic solution [Eq. (31)].

4.2. Numerical results for slick water fracturing

The proposed model is now employed to analyze the residual opening and conductivity of a fracture with a basal (non-symmetric) bank. This is typical for slick water fracturing where low fluid viscosity (water) allows relatively rapid settling.

First, a base case is examined to demonstrate the proposed model. Consider a blade-shaped fracture with a height H of 10 m that is subjected to a far-field stress σ_h of 20 MPa. The surrounding formation has a plane strain Young's modulus E' of 25 GPa. The initial internal fluid pressure, p_0 , is assumed uniform over the fracture height and is 24.77 MPa (at the end of pumping), corresponding to an initial average fracture width \bar{w}_0 of 3 mm. The initial reservoir pore pressure, p_{rsv} , is assumed to be 15 MPa. In this case, it is assumed that all of the proppant settles to the fracture base and forms a bed with a height h of 5 m, i.e. the initial normalized proppant concentration satisfies $\bar{c}_0(z \leq 0) = 1$ and $\bar{c}_0(z > 0) = 0$. The initial shape of the fracture and the initial concentration distribution of the proppant are shown in Fig. 8(a) and (b), respectively. The other input parameters are given in Table 2. A large number of spatial collocation points, $N = 100$, are used for the numerical solution to ensure that sudden changes of quantities can be captured with sufficient resolution.

Fig. 8(c)–(g) show the evolution of the fracture width profile, w , the compacting stress on the proppant pack, σ_p , the proppant embedment, w_e , and the fracture conductivity, C , on both natural and logarithmic scales, as the fluid pressure within the fracture gradually declines. It can be seen from Fig. 8(c) that, during the shut-in stage, as the fluid pressure decreases from the initial pressure (24.77 MPa) to the reservoir pore pressure (15 MPa), the upper unpropped portion of the fracture closes gradually onto the asperities under the closure pressure, while the lower propped portion shows only a slight decrease in width due to the compaction of the proppant pack. An arch zone with a height of ~ 2 m is formed just above the top of the proppant bed. During production, as the fluid pressure decreases from the initial reservoir pore pressure (15 MPa) to 0 MPa, the width of the propped fracture decreases slowly, and a reduction of the height of the arch zone is also observed – reducing it to ~ 0.6 m when the pressure is completely depleted. The compacting stress applied on the proppant pack increases as the fluid pressure decreases, as shown in Fig. 8(d). This stress is relatively constant near the bottom of the fracture, which is slightly larger than the value of $p_0 - p$, but increases rapidly as the top of the proppant bed is approached – this is to support the arch zone. The maximum value of the compacting stress, which is ~ 3 times as large as that in the lower region, is reached at the top of the proppant bed, where low-strength proppant particles might crush and be produced through the open-arch zone if there is a reasonable connection in the perforations. Thus, a “tail-in” of high strength proppant might be beneficial to reduce proppant crushing and to maintain the arch zone. Since that the depth of proppant embedment is proportional to the compacting stress to the power of $2/3$ [Eq. (16)], the evolution of proppant embedment has a similar trend to that of the compacting stress as fluid pressure decreases, as shown in Fig. 8(e). Proppant embedment remains relatively constant in the basal region of the fracture, and increases quickly and reaches a peak at the top of the bed where the largest compacting stress results. Fig. 8(g) shows that the conductivity of the proppant bed is comparatively constant over the entire bed height except for the two endpoints, i.e., the base and the top of the proppant bed. The smaller conductivity in the base results from the narrower fracture width, while that at the top is due to the more highly compacted pack with a reduced porosity. The closed unpropped part of the fracture has a conductivity ~ 3 orders of magnitude lower than that of the proppant bed. However, the open-arch zone adjacent to the top of the proppant bed exhibits an extremely high conductivity which is ~ 2 – 3 orders of magnitude larger than that of the proppant bed. This high-conductivity pathway may be beneficial during cleanup and production, but may also aid in enhancing proppant flowback. As the internal fluid pressure declines, the overall conductivity of the fracture decreases due to

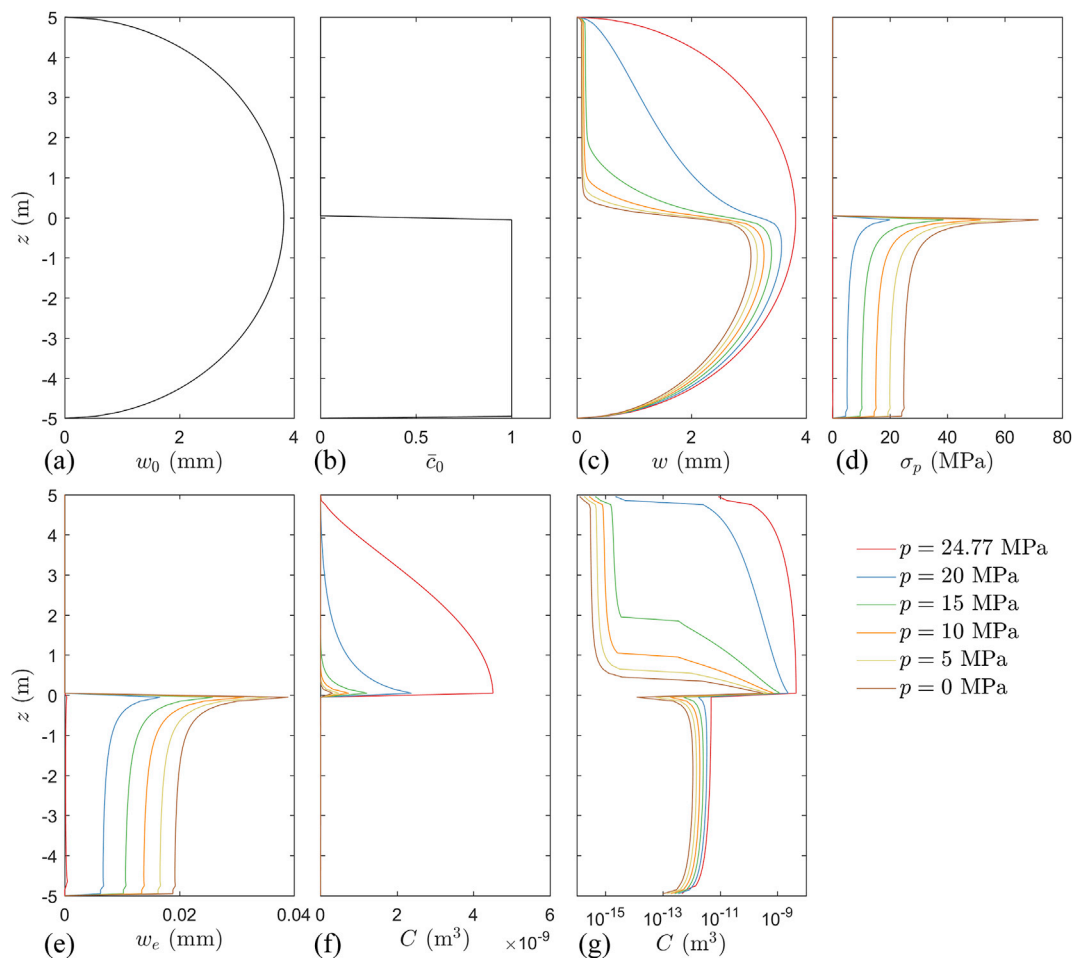


Fig. 8. Initial conditions and simulation results of the base case: (a) the initial shape of the fracture; (b) the initial distribution of the normalized proppant concentration; and the evolution of (c) the fracture width, (d) the compacting stress on proppant pack, (e) the proppant embedment, and the fracture conductivity (f) and (g) in logarithmic scale as fluid pressure decreases. (The initial fluid pressure within the fracture is 24.77 MPa, and the initial pore pressure of the reservoir is 15 MPa.)

Table 2
Input parameters for the base case.

Parameters	Values
Fracture height, H	10 m (Detournay et al., 1990)
Far-field stress, σ_h	20 MPa (Shiozawa and McClure, 2016)
Initial averaged fracture width, \bar{w}_0	3 mm (Palisch et al., 2010)
Plane strain Young's modulus, E'	25 GPa (Dontsov and Peirce, 2015)
Initial fluid pressure, p_0	24.77 MPa [back-calculated from H , σ_h , E' and \bar{w}_0 based on Eq. (31)]
Initial reservoir pore pressure, p_{rsv}	15 MPa (Shiozawa and McClure, 2016)
Compressibility of proppant pack, c_p	$7.25 \times 10^{-9} \text{ Pa}^{-1}$ (Shiozawa and McClure, 2016)
Asperity width, w_a	0.1 mm (Bandis et al., 1983)
Asperity compliance, b_1	$1.43 \times 10^{-10} \text{ Pa}^{-1}$
Proppant radius, R	0.4 mm (Palisch et al., 2010)
Maximum proppant concentration, c_{max}	0.53

compaction of the proppant bed and the reduced size of the open-arch zone.

Cases with different proppant bed height are examined for the same general fracture conditions that were specified previously (Table 2). These calculations are performed when the internal fluid pressure $p = 5$ MPa, and the ratio of bed height to fracture height, h/H , ranges from

0.2 to 1.0, as shown in Fig. 9(a). It can be seen from Fig. 9(b) that arch zones form in the four cases for $h/H < 1$ and are not observed in the case where the fracture is fully filled by proppant ($h/H = 1$). The height of the arch zone for the case of $h/H = 0.2$ is ~ 0.4 m, and that for the cases of $h/H = 0.4, 0.6$ and 0.8 is ~ 0.6 m. This indicates that the height of the arch zone only changes slightly as the bed height changes significantly and reaches maximum value at this intermediate value of fill height. Due to this similarity in arch zone dimensions, the conductivities of the arch zones for the cases of $h/H < 1$ also show similar magnitude, as can be seen from Fig. 9(d). Fig. 9(c) shows that the compacting stress exhibits a monotonically decreasing trend with increasing bed height. Thus, under the same fracture conditions, particles within a less high proppant bed may experience greater embedment into the fracture walls and/or a larger potential of crushing.

Another set of cases with different initial fracture widths ($\bar{w}_0 = 1$ mm, 3 mm and 5 mm) is examined with the remaining input parameters identical to those listed in Table 2. The initial fracture shapes are shown in Fig. 10(a), and the initial proppant concentration distribution is the same as that shown in Fig. 8(b), i.e., the proppant bed height is 5 m for all the three cases. Note that a wider initial fracture indicates a larger amount of proppant filling in the fracture. When the internal fluid pressure decreases to 5 MPa, the residual aperture profiles are shown in Fig. 10(b). A larger initial fracture width results in a larger residual opening due to a greater mass (initial width) of proppant filling the fracture and propping it open. The heights of the arch zones for the cases of $\bar{w}_0 = 1$ mm, 3 mm and 5 mm are 0.1 m, 0.6 m and 1.0 m, respectively.

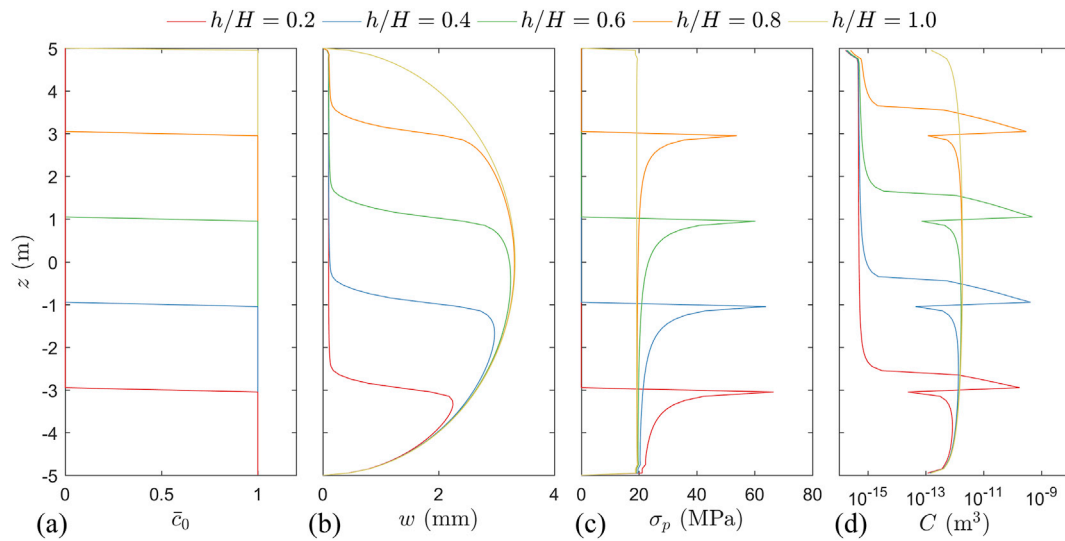


Fig. 9. Cases with various proppant bed heights: (a) initial proppant distributions; (b) residual opening profiles; (c) resultant compacting stresses applied on proppant bed; and (d) fracture conductivities after fracture closure. [The initial fracture shape is identical to that shown in Fig. 8(a), and the internal fluid pressure is 5 MPa].

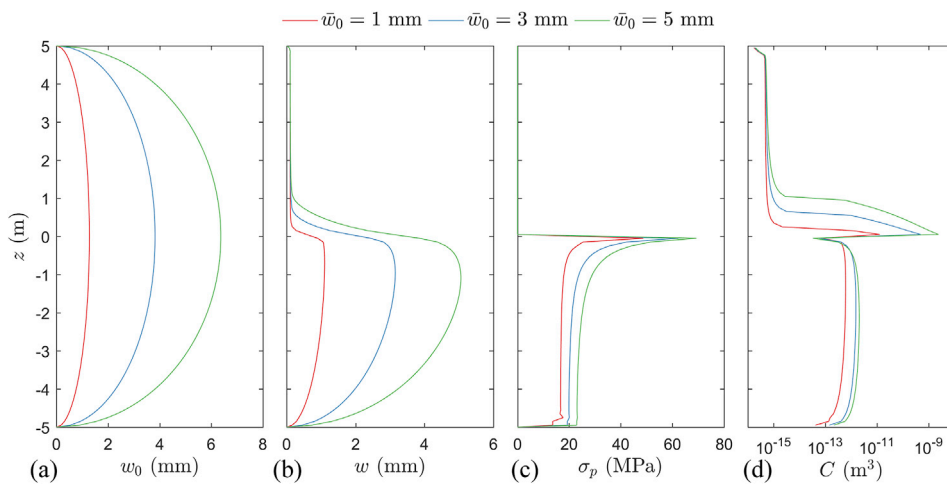


Fig. 10. Cases with various initial fracture widths: (a) initial fracture shapes; (b) residual opening profiles; (c) resultant compacting stresses applied on the proppant bed; and (d) fracture conductivities after fracture closure. [The initial proppant concentration distribution is the same as that shown in Fig. 8(b), and the internal fluid pressure is 5 MPa].

A larger dimension of the arch zone in turn results in a pathway with greater conductivity, as shown in Fig. 10(d). However, larger residual opening requires higher stress to maintain the shape of the fracture, as indicated by Eqs. (1) and (2). Therefore, the case of $\bar{w}_0 = 5$ mm shows the highest overall compacting stress while the case of $\bar{w}_0 = 1$ mm shows the lowest, as can be seen from Fig. 10(c).

To examine the impact of elastic modulus of the formation on the resulting fracture residual opening, three cases with different plane strain Young's moduli ($E' = 5$ GPa, 25 GPa and 45 GPa) are considered. The other input parameters are, again, the same as the base case (Table 2). Fig. 11(a) shows that a smaller elastic modulus of the formation results in a less compacted proppant bed but a smaller arch zone. This is due to the condition that a lower stress will result in a larger fracture dilation in a softer formation (Fig. 11(b)), but a narrower arch zone dimension. As a result, the case for $E' = 5$ GPa has the smallest conductivity for the arch zone, although it shows a slightly higher conductivity for the proppant bed than the other two cases since it is the least compacted (Fig. 11(d)). Fig. 11(c) shows the proppant embedment for those three cases. It can be seen that, despite the fact that the lowest compacting stress is applied on the proppant bed for the case of $E' = 5$ GPa (Fig. 11(b)), this case experiences the largest proppant embedment due to the most compliant fracture walls.

Sometimes rapid leak-off of fracturing fluid or rough and tortuous fractures may preclude the complete settling of proppant before a fracture closes. In such a case, the initial proppant concentration distribution may be similar to that shown in Fig. 12(a) where two proppant packs are formed with different initial concentrations. Calculations are performed with this initial proppant distribution. The input parameters are identical to those listed in Table 2. Fig. 12(b) and (c) show the residual opening profile, compacting stress acting on the proppant pack, and the fracture conductivity after fracture closure, respectively, when the internal fluid pressure decreases to 5 MPa. Two arch zones are formed between the two discontinuities of the proppant concentration (Fig. 12(b)). Both arch zones have a higher relative conductivity than the compacted proppant packs (Fig. 12(d)). Extremely high compacting stresses are observed at the top of each proppant pack, as shown in Fig. 12(c). Note that the compacting stress is zero within the lower arch zone, indicating that the proppant in that region has not been compacted. That proppant will ultimately settle down to the top of the lower proppant pack and may be mobile during cleanup and production – likely contributing to proppant flowback under sufficiently high flow rates.

It is commonly believed that a uniform proppant distribution is favored for optimal well performance (Palisch et al., 2010). However, according to the above analysis, the resulting arch zone next to the

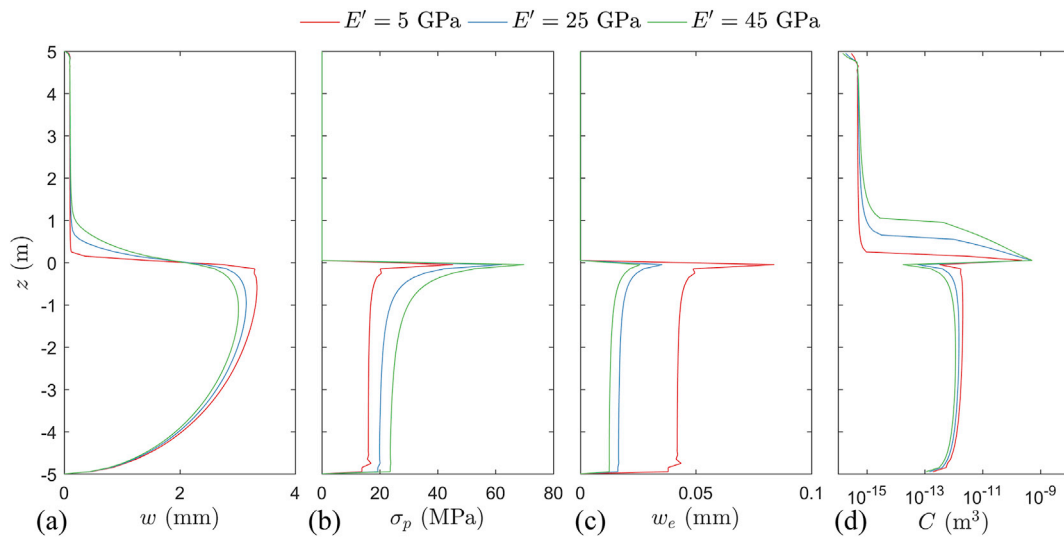


Fig. 11. Cases with various plane strain Young's modulus of the formation: (a) residual opening profiles; (b) resultant compacting stresses applied on proppant bed; (c) proppant embedment; and (d) fracture conductivities after fracture closure. [The initial fracture shape and proppant concentration distribution are same as those shown in Fig. 8(a) and (b), respectively, and the internal fluid pressure is 5 MPa].

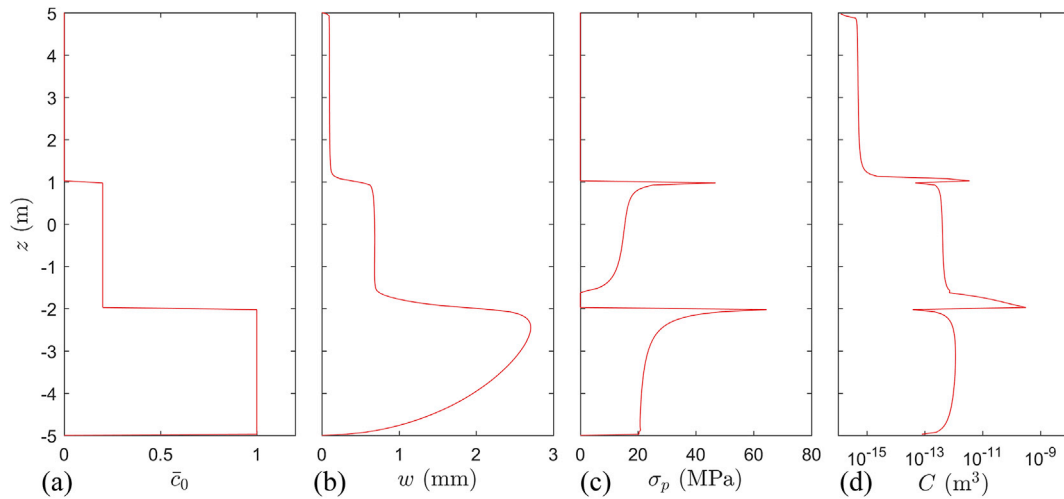


Fig. 12. Case with part of the proppant stranded above the proppant bed: (a) initial proppant concentration distribution; (b) residual opening profile; (c) resultant compacting stress applied on proppant packs; and (d) fracture conductivity after fracture closure. [The initial fracture shape is the same as the one shown in Fig. 8(a), and the internal fluid pressure is 5 MPa].

proppant bed can offer a high-conductivity pathway for fluids to be recovered, while the unpropped and closed zone above it has a relatively low conductivity. Therefore, it is feasible that an optimal proppant distribution may exist that can maximize the fracture transmissivity with a given mass of proppant injected. This is explored by employing five idealized initial proppant distributions with the same total volume of proppant. In these five cases, proppant packs are formed with different heights, h , and initial concentrations, \bar{c}_0 , as shown in Fig. 13(a). The initial proppant concentrations for cases of $h/H = 0.3, 0.5, 0.7, 0.9$ and 1.0 are $\bar{c}_0 = 1, 0.505, 0.338, 0.266$ and 0.252 , respectively. Thus, the case of $h/H = 0.3$ represents the condition that all of the proppant settle to the base of the fracture, while the case of $h/H = 1.0$ corresponds to a uniform proppant distribution. The other input parameters are identical to the base case (Table 2). Fig. 13(b) shows the residual opening profiles for these five cases. Since the total volume of proppant is the same, the width of the propped zone decreases as the proppant pack height increases, resulting in a decreasing arch zone dimension. However, the height of the unpropped, closed zone also decreases as the proppant distributes more uniformly. The resultant conductivity is shown in

Fig. 13(d), and the fracture transmissivity can be calculated as

$$T = \int_{-H/2}^{H/2} C(z) dz. \tag{31}$$

Fig. 14 shows the calculated fracture transmissivity as a function of proppant pack height for these five cases. It is apparent that cases with shorter and wider proppant packs have higher fracture transmissivity if the total volume of the proppant is the same. This is attributed to the larger arch zones. According to the above analysis, it is plausible that the case with all of the proppant settling to the base of the fracture is more desirable than the case with a uniform proppant distribution. Negating this argument is that the top of the formation is vertically unconnected to the open-arch zone and this may increase the diffusion length of reservoir fluids during production. Production simulations are needed to examine the performance of wells with those different fracture conductivities. In addition, the sustainability of the arch zone should be examined as well since higher compacting stress is observed for cases with lower proppant pack height [Fig. 13(c)] and this may crush the proppant particles and diminish the extent of the arch zone.

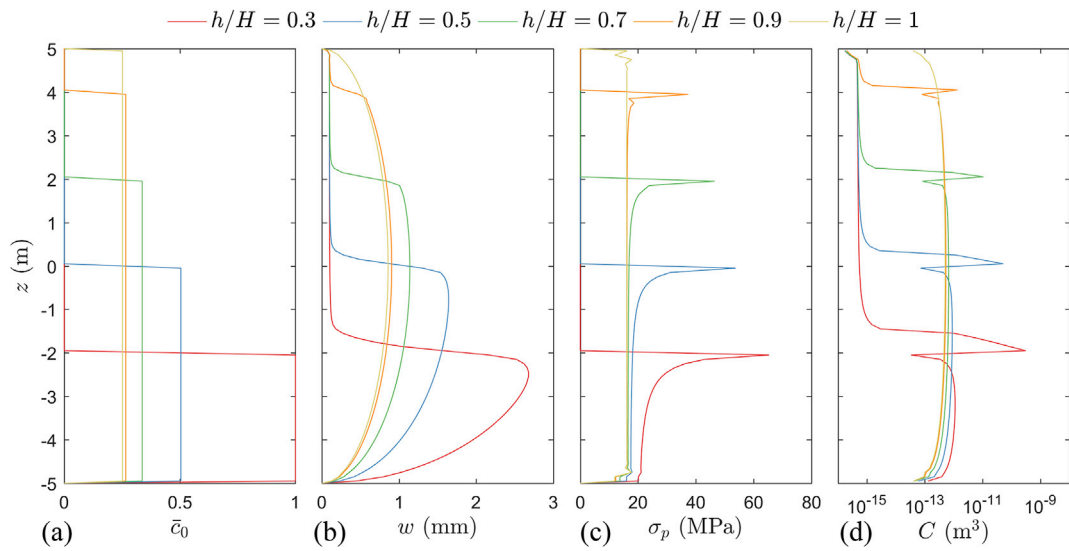


Fig. 13. Cases with the same total volume of proppant but different proppant pack: (a) initial proppant concentration distributions; (b) residual opening profiles; (c) resultant compacting stresses applied on proppant packs; and (d) fracture conductivities after fracture closure. [The initial fracture shape is the same as the one shown in Fig. 8(a), and the internal fluid pressure is 5 MPa].

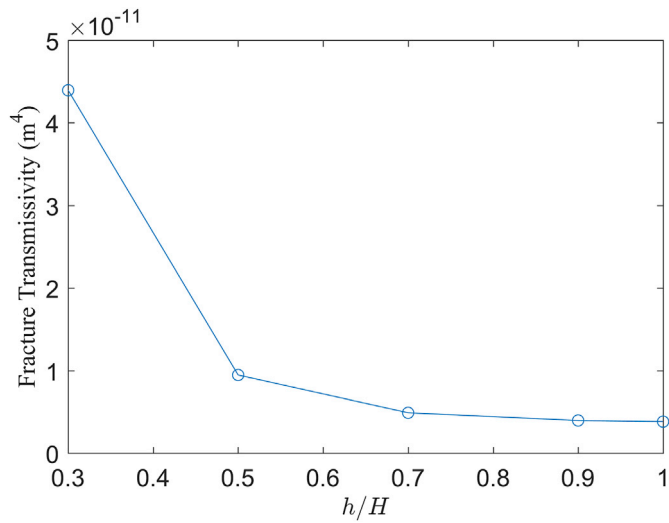


Fig. 14. Fracture transmissivity as a function of the ratio of proppant pack height to fracture height. (The total volume of proppant remains constant.)

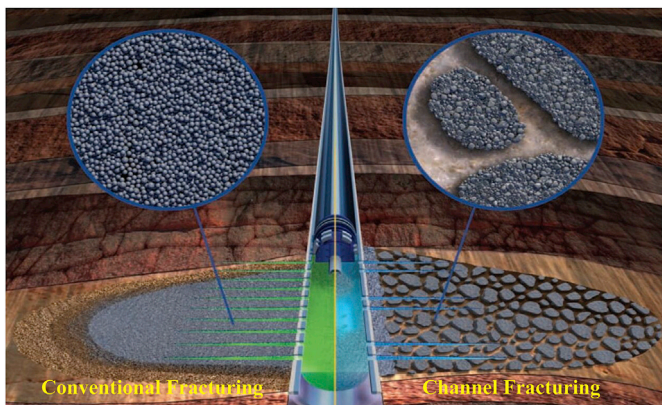


Fig. 15. Schematic of proppant distribution in conventional fracturing (left) and channel fracturing (right). (D'Huteau et al., 2011).

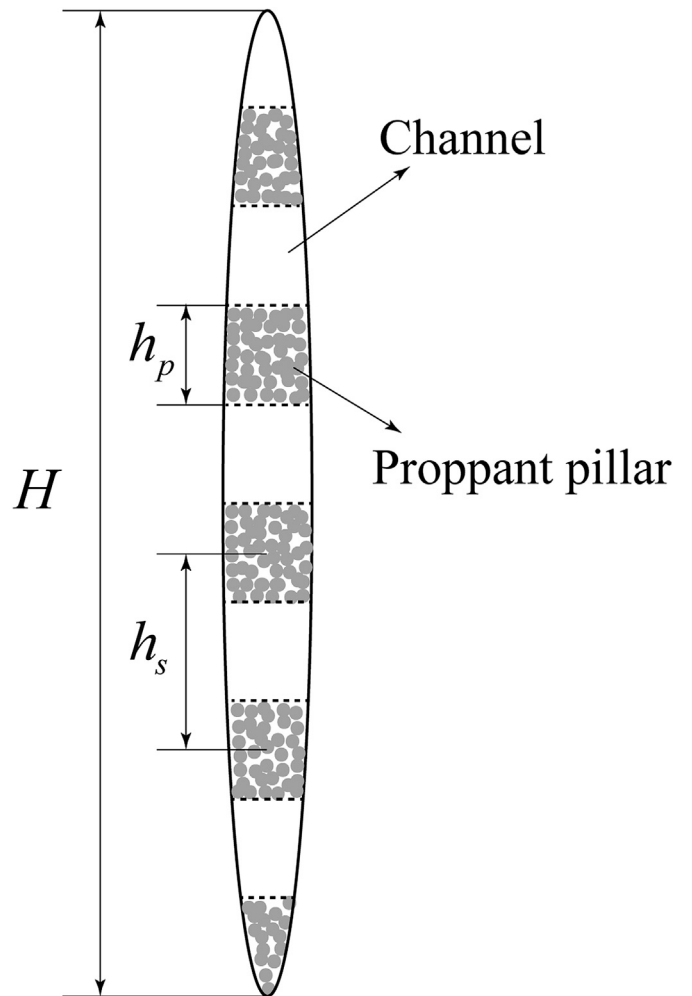


Fig. 16. Schematic of a simplified 2D case of channel fracturing.

4.3. Numerical results for channel fracturing

Channel fracturing is an emerging technique which enables fractures to be propped by discontinuous proppant pillars. This creates a network of high-conductivity, open channels within the fractures, as shown in Fig. 15. This new technique stems from combining the concepts of partial monolayer fracturing (Brannon et al., 2004) and periodic propped fracturing (Tinsley and Williams, 1975). This has been widely applied over the past several years (Gillard et al., 2010; Medvedev et al., 2013). In channel fracturing, an inhomogeneous placement of proppant is achieved by injecting a train of proppant-laden then proppant-free fluids into the well and fracture and using degradable fibers that can wrap the proppants and prevent dispersion of the proppant pulses. Several models have been developed to explore fracture conductivity after channel fracturing (Zheng et al., 2017; Yan et al., 2016; Guo et al., 2017). These

models assume that the channels remain open throughout the well life. However, this may not be the case in reality where the channels may close under high stress, resulting in a reduction of the fracture conductivity.

In this subsection, our proposed model is used to analyze the residual aperture and conductivity of the fractures produced by channel fracturing in a simple 2D case (Fig. 16). It is assumed that the proppant pillars have a uniform height, h_p , and are distributed in the fracture with an even spacing, h_s . In this set of simulations, the number of proppant pillars in the fracture is set to be 5, i.e. $h_p \leq h_s = H/5$, and different ratios of proppant pillar height to spacing, h_p/h_s , are considered, ranging from 0 to 1. The other input parameters are the same as those listed in Table 2. Fig. 17 show the three different initial proppant concentration distributions used here, with the ratio of proppant pillar height to spacing $h_p/h_s = 0.3, 0.7$ and 0.9 , respectively. The calculations are conducted

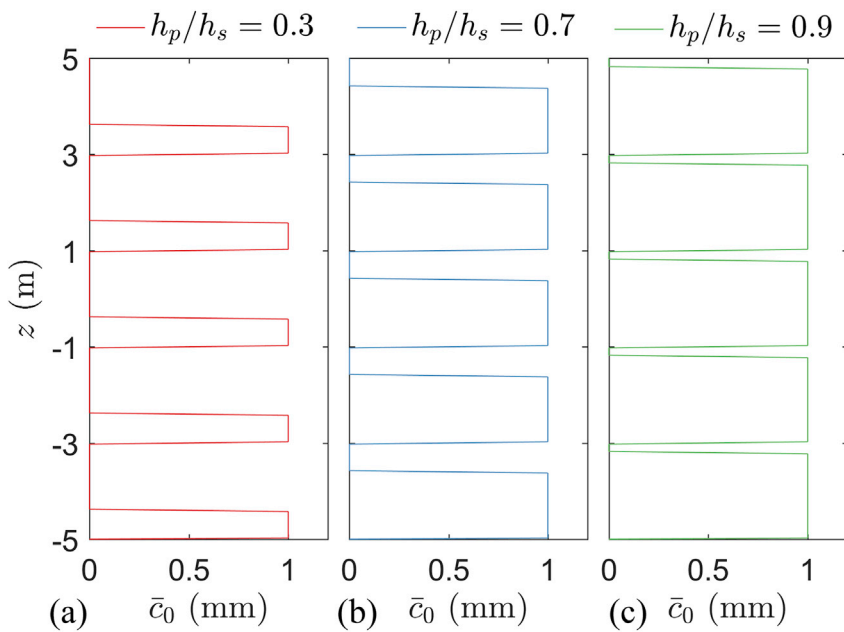


Fig. 17. Initial proppant concentration distributions with different ratios of proppant pillar height to spacing: (a) $h_p/h_s = 0.3$, (b) $h_p/h_s = 0.7$, and (c) $h_p/h_s = 0.9$.

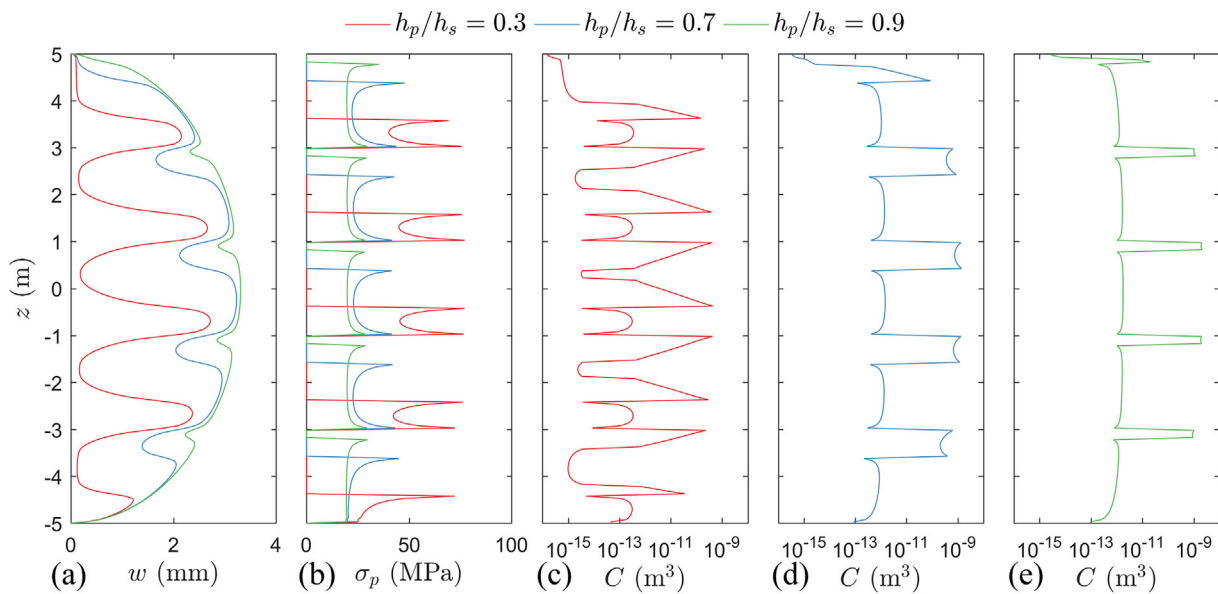


Fig. 18. Simulation results for the cases of channel fracturing with different ratios of proppant pillar height to spacing: (a) residual opening profiles; (b) resultant compacting stresses applied on proppant packs; and fracture conductivities after fracture closure for cases of (c) $h_p/h_s = 0.3$, (d) $h_p/h_s = 0.7$, and (e) $h_p/h_s = 0.9$. [The initial fracture shape is the same as that shown in Fig. 8(a), and the internal fluid pressure is 5 MPa].

assuming that the fluid pressure is depleted to 5 MPa (Fig. 18). For the case of $h_p/h_s = 0.3$, the fracture walls contact midway between the proppant pillars (Fig. 18(a)) where the fracture is closed to the fluid flow, as indicated by the extremely low conductivity in Fig. 18(c). In addition, proppant pillars in this case ($h_p/h_s = 0.3$) experience higher compacting stress (Fig. 18(b)) than the other two cases, especially in the pillar edge regions. These in turn decrease the conductivity of the proppant packs, lowering the overall fracture transmissivity. For the case of $h_p/h_s = 0.7$, the channel is still open with a reasonable width showing a flow capacity several orders of magnitude greater than that of the proppant pillars. The fracture transmissivity of this case is much higher than that of the case for $h_p/h_s = 0.3$. The case for $h_p/h_s = 0.9$ is similar to that for $h_p/h_s = 0.7$, but the proppant pillars are much closer together and the distance over which the fracture remains open is shorter. This suggests that more of the fracture surface is propped than may be necessary. Therefore, there appears to be an optimal ratio of proppant pillar height to spacing that will result in the maximum fracture transmissivity after fracture closure. Fig. 19 plots the fracture transmissivity as a function of the ratio of proppant pillar height to spacing. This shows that the maximum fracture transmissivity is reached when h_p/h_s is ~ 0.8 .

5. Conclusions

A 2D model has been developed to obtain the residual opening and conductivity of hydraulic fractures filled with arbitrarily distributed proppant packs. This model is based on a 2D elasticity integral equation with a Cauchy-type singular kernel that incorporates the non-local effect of the local ensemble normal stress across the height of the fracture. It is capable of accommodating the mechanical response of proppant packs,

fracture closure on rough surfaces, and proppant embedment into fracture walls. The conductivity of the closed, partially/fully propped fracture is derived from the cubic law and the Kozeny–Carman permeability model.

Proppant beds are assumed to accumulate at the base of hydraulic fractures if low-viscosity fracturing fluids are used for stimulation. During cleanup and production, reduced fluid pressure within the fracture leads to compaction of the proppant packs as well as only the partial closure of unpropped fracture portions. An open-arched zone is necessarily formed next to the proppant pack. The dimensions of the arched zones decrease as the fluid pressure declines, and it is also limited by the small proppant mass filling the fracture and by the low elastic modulus of the formation. The proppant bed height has little impact on the extent of the arched zone if bed height is neither close to zero or the fracture height. The arched zones have extremely high conductivity compared with the compacted proppant beds and the closed, unpropped fracture portions. This high-conductivity pathway may have a significant impact on cleanup, production and proppant flowback. However, higher compacting stress and greater proppant embedment are observed at the top of the proppant bed, which may be disadvantageous to sustaining the arch zone.

Contrary to conventional wisdom, simulations suggest that, for a given mass of proppant, uniform distribution throughout the full height of the fracture may not be as effective as a wedge at the fracture base with an open-arch formed above. This arched zone results in a higher overall fracture transmissivity than a uniform proppant distribution. However, this may require further demonstration by production simulations since part of the pay-zone might be disconnected from, or poorly-connected to, the preferential pathway for fluid flow, and this may increase the hydrocarbon diffusion length.

The proposed model is also applied to analyze the fracture conductivity of channel fracturing in a simple 2D representation. Simulation results show that the open channels formed between proppant pillars could improve fracture transmissivity dramatically - if they are maintained throughout the life of the well. However, for a fixed proppant pillar height, a large proppant pillar spacing could lead to the premature closure of the flow channels, while a small pillar spacing may narrow those channels. An optimal ratio of proppant pillar height to spacing should maximize the overall fracture transmissivity during production.

Acknowledgement

This work is the result of support from DOE under the Small Business Innovation Research program (grant number: DE-SC0013217). This support is gratefully acknowledged.

Appendix

For a proppant layer in contact with a fracture wall, the densest packing is a hexagonal lattice, as shown in Fig. 20 (a). Fig. 20 (b) plots

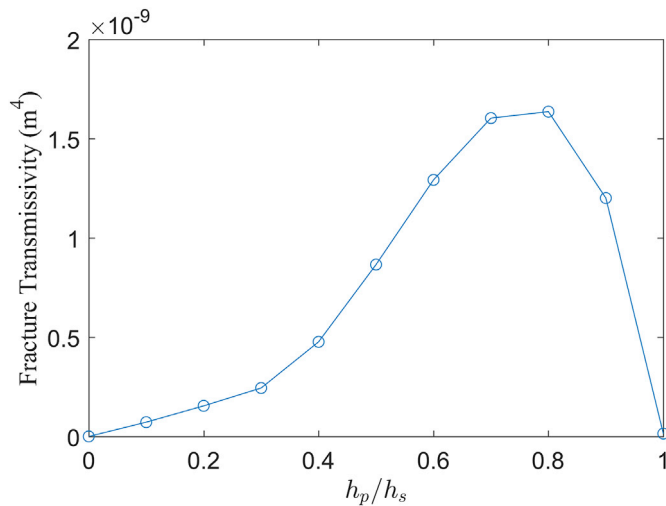


Fig. 19. Fracture transmissivity as a function of the ratio of proppant pillar height to spacing.

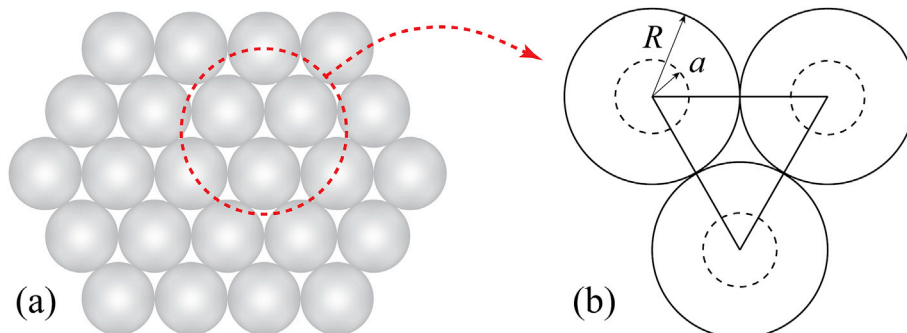


Fig. 20. Proppant packing for the layer in contact with a fracture wall: (a) hexagonal lattice, and (b) three adjacent proppant particles (solid-line circles) and contact zones between particles and the fracture wall (dashed-line circles).

three adjacent proppant particles (solid-line circles) and contact zones between particles and the fracture wall (dashed-line circles), where R and a represent radii of the particle and the contact zone, respectively. The equilateral triangle shown in Fig. 20 (b) has an area of $\sqrt{3}R^2$ and overlaps the contact zones with an area of $\pi a^2/2$. Thus, the mean contact pressure, $p_m(z)$, and the compacting stress, $\sigma_p(z)$, are related as

$$p_m(z)\pi a^2 = 2\sqrt{3}\sigma_p(z)R^2. \quad (32)$$

Therefore, the constant η in Eq. (14) is $2\sqrt{3}$ for the densest packing type (hexagonal lattice), and $\eta > 2\sqrt{3}$ for other looser ones.

Nomenclature

H	Fracture height (m)
E	Young's modulus (GPa)
ν	Poisson's ratio (–)
E'	Plane strain Young's modulus (GPa)
σ_n	Ensemble stress (MPa)
σ_p	Compacting stress on proppant pack (MPa)
σ_a	Back stress from fracture asperities (MPa)
σ_h	Far-field stress (MPa)
p	Fluid pressure within fracture (MPa)
p_0	Initial fluid pressure within fracture (MPa)
p_{rsv}	Initial reservoir pore pressure (MPa)
w	Fracture width (mm)
w_0	Initial fracture width (mm)
\bar{w}_0	Initial averaged fracture width (mm)
w_e	Depth of proppant embedment (mm)
G	Elastic kernel (–)
c_0	Initial proppant volumetric concentration (–)
c_{max}	The maximum value of initial proppant volumetric concentration (–)
\bar{c}_0	Normalized initial proppant concentration (–)
w_{p0}	Initial width of proppant pack (mm)
c_p	Compressibility of proppant pack (Pa^{-1})
w_{a0}	Asperity width (mm)
b_1	Asperity compliance (Pa^{-1})
b_2	Constant determined by asperity width and compliance (–)
a	Radius of contact zone (mm)
R	Radius of proppant particle (mm)
P	Indenter load (MPa)
E^*	Combined modulus of indenter and half-space (GPa)
p_m	Mean contact pressure (MPa)
u_r	Vertical normal displacement (mm)
η	Proppant packing constant (–)
k_f	Permeability of unpropped fracture (m^2)
k_p	Permeability of compacted proppant pack (m^2)
ϕ_p	Porosity of compacted proppant pack (–)
k_K	Kozeny-Carman constant (–)
S_{Vgr}	Total particle surface area per unit volume of solid phase (m^{-1})
\hat{Q}^s	Function representing slurry mobility (–)
k'_f	Permeability of unpropped fracture containing uncompacted proppant (m^2)
C	Fracture conductivity (m^3)
h	Height of proppant bed (m)
T	Fracture transmissivity (m^4)
h_p	Height of proppant pillar (m)
h_s	Spacing between proppant pillars (m)

References

- Adachi, J., Siebrits, E., Peirce, A., Desroches, J., 2007. Computer simulation of hydraulic fractures. *Int. J. Rock Mech. Min. Sci.* 44, 739–757. <https://doi.org/10.1016/j.ijrmms.2006.11.006>.
- Alramahi, B., Sundberg, M.I., 2012. Proppant embedment and conductivity of hydraulic fractures in shales. In: 46th US Rock Mech. Symp. <https://doi.org/10.1016/j.ijengsci.2013.12.005>.
- Bandis, S.C., Lumsden, A.C., Barton, N.R., 1983. Fundamentals of rock joint deformation. *Int. J. Rock Mech. Min. Sci.* 20, 249–268. [https://doi.org/10.1016/0148-9062\(83\)90595-8](https://doi.org/10.1016/0148-9062(83)90595-8).
- Barton, N., Bandis, S., Bakhtar, K., 1985. Strength, deformation and conductivity coupling of rock joints. *Int. J. Rock Mech. Min. Sci.* 22, 121–140. [https://doi.org/10.1016/0148-9062\(85\)93227-9](https://doi.org/10.1016/0148-9062(85)93227-9).
- Brady, B.H.G., Brown, E.T., 2006. *Rock Mechanics for Underground Mining*, third ed. Springer <https://doi.org/10.1007/978-1-4020-2116-9>.
- Brannon, H.D., Malone, M.R., Rickards, A.R., Wood, W.D., Edgeman, J.R., Company, B.J.S., Bryant, J.L., Corp, A.H., 2004. Maximizing fracture conductivity with proppant partial monolayers: theoretical curiosity or highly productive reality?. In: SPE Annual Technical Conference and Exhibition. Society of Petroleum Engineers. <https://doi.org/10.2118/90698-MS>.
- Carman, P.C., 1937. Fluid flow through granular beds. *Trans. Chem. Eng.* 15, 150–166.
- Chen, D., Ye, Z., Pan, Z., Zhou, Y., Zhang, J., 2017. A permeability model for the hydraulic fracture filled with proppant packs under combined effect of compaction and

- embedment. *J. Pet. Sci. Eng.* 149, 428–435. <https://doi.org/10.1016/j.petrol.2016.10.045>.
- Cipolla, C.L., Lolon, E.P., Ceramics, C., Mayerhofer, M.J., Warpinski, N.R., Technologies, P., 2009. The effect of proppant distribution and un-propped fracture conductivity on well performance in unconventional gas reservoirs. *psi. Spe* 1–10. <https://doi.org/10.2118/119368-MS>.
- Cleary, M., 1980. Analysis of mechanisms and procedures for producing favourable shapes of hydraulic fractures. In: *SPE Annual Technical Conference and Exhibition*. Society of Petroleum Engineers. <https://doi.org/10.2118/9260-MS>.
- Crouch, S.L., 1976. Solution of plane elasticity problems by the displacement discontinuity method. *Int. J. Numer. Methods Eng.* 10, 301–343. <https://doi.org/10.1002/nme.1620100206>.
- D'Huteau, E., Gillard, M., Miller, M., Peña, A., Johnson, J., Turner, M., Medvedev, O., Rhein, T., Willberg, D., 2011. Open-channel fracturing — a fast track to production. *Oilf. Rev.* 1–14.
- Daneshy, A.A., 1978. Numerical solution of sand transport in hydraulic fracturing. *J. Pet. Technol.* 30, 132–140.
- Detournay, E., 2016. Mechanics of hydraulic fractures. *Annu. Rev. Fluid Mech.* 48, 311–339. <https://doi.org/10.1146/annurev-fluid-010814-014736>.
- Detournay, E., Cheng, A.H.-D., McLennan, J.D., 1990. A poroelastic PKN hydraulic fracture model based on an explicit moving mesh algorithm. *J. Energy Resour. Technol.* 112, 224. <https://doi.org/10.1115/1.2905762>.
- Dontsov, E.V., Peirce, A.P., 2015. Proppant transport in hydraulic fracturing: crack tip screen-out in KGD and P3D models. *Int. J. Solids Struct.* 63, 206–218. <https://doi.org/10.1016/j.jsolstr.2015.02.051>.
- Dontsov, E.V., Peirce, a. P., 2014. Slurry flow, gravitational settling and a proppant transport model for hydraulic fractures. *J. Fluid Mech.* 760, 567–590. <https://doi.org/10.1017/jfm.2014.606>.
- Economides, M.J., Nolte, K.G., 2000. In: *Reservoir Stimulation*, vol. 18. Wiley, New York.
- Fischer-Cripps, A.C., 2007. *Introduction to Contact Mechanics*. Springer Science & Business Media, New York. <https://doi.org/10.1007/b22134>.
- Gillard, M.R., Medvedev, O.O., Hosein, P.R., Medvedev, A., Peñacorada, F., D'Huteau, E., 2010. A new approach to generating fracture conductivity. In: *SPE Annual Technical Conference and Exhibition*. Society of Petroleum Engineers. <https://doi.org/10.2118/135034-MS>.
- Gu, M., Mohanty, K.K., 2014. Effect of foam quality on effectiveness of hydraulic fracturing in shales. *Int. J. Rock Mech. Min. Sci.* 70, 273–285. <https://doi.org/10.1016/j.ijrmms.2014.05.013>.
- Guo, J., Wang, J., Liu, Y., Chen, Z., Zhu, H., 2017. Analytical analysis of fracture conductivity for sparse distribution of proppant packs. *J. Geophys. Eng.* 14, 599–610. <https://doi.org/10.1088/1742-2140/aa6215>.
- Kern, L.R., Perkins, T.K., Wyant, R.E., 1959. The mechanics of sand movement in fracturing. *J. Pet. Technol.* 11, 55–57. <https://doi.org/10.2118/1108-G>.
- Khanna, A., Kotousov, A., Sobey, J., Weller, P., 2012. Conductivity of narrow fractures filled with a proppant monolayer. *J. Pet. Sci. Eng.* 100, 9–13. <https://doi.org/10.1016/j.petrol.2012.11.016>.
- Khanna, A., Neto, L.B., Kotousov, A., 2014. Effect of residual opening on the inflow performance of a hydraulic fracture. *Int. J. Eng. Sci.* 74, 80–90. <https://doi.org/10.1016/j.ijengsci.2013.08.012>.
- Kozeny, J., 1927. *Über Kapillare Leitung der Wasser in Boden*. *R. Acad. Sci. Vienna, Proc. Cl. I* 136, 271–306.
- Lee, D.S., Elsworth, D., Yasuhara, H., Weaver, J.D., Rickman, R., 2010. Experiment and modeling to evaluate the effects of proppant-pack diagenesis on fracture treatments. *J. Pet. Sci. Eng.* 74, 67–76. <https://doi.org/10.1016/j.petrol.2010.08.007>.
- Liu, Y., Leung, J.Y., Chalaturmyk, R., Virues, C.J.J., Ulc, N.E., 2017. Fracturing fluid distribution in shale gas reservoirs due to fracture closure, proppant distribution and gravity segregation. In: *SPE Unconventional Resources Conference*.
- McLennan, J.D., Green, S.J., Bai, M., 2008. Proppant placement during tight gas shale Stimulation: literature review and speculation. In: *The 42nd US Rock Mechanics Symposium*. American Rock Mechanics Association.
- Medvedev, A., Kraemer, C., Pena, A., Panga, M., 2013. On the mechanisms of channel fracturing. In: *SPE Hydraulic Fracturing Technology Conference*. Society of Petroleum Engineers. <https://doi.org/10.2118/163836-MS>.
- Neto, L.B., Khanna, A., Kotousov, A., 2015. Conductivity and performance of hydraulic fractures partially filled with compressible proppant packs. *Int. J. Rock Mech. Min. Sci.* 74, 1–9. <https://doi.org/10.1016/j.ijrmms.2014.11.005>.
- Neto, L.B., Kotousov, A., 2013a. Residual opening of hydraulic fractures filled with compressible proppant. *Int. J. Rock Mech. Min. Sci.* 61, 223–230. <https://doi.org/10.1016/j.ijrmms.2013.02.012>.
- Neto, L.B., Kotousov, A., 2013b. On the residual opening of hydraulic fractures. *Int. J. Fract.* 181, 127–137. <https://doi.org/10.1007/s10704-013-9828-1>.
- Nordgren, R.P., 1972. Propagation of a vertical hydraulic fracture. *Soc. Pet. Eng. J.* 12, 306–314. <https://doi.org/10.2118/3009-PA>.
- Osipov, A.A., 2017. Fluid mechanics of hydraulic fracturing: a review. *J. Pet. Sci. Eng.* 156, 513–535. <https://doi.org/10.1016/j.petrol.2017.05.019>.
- Ouyang, S., Carey, G.F., Yew, C.H., 1997. An adaptive finite element scheme for hydraulic fracturing with proppant transport. *Int. J. Numer. Methods Fluids* 24, 645–670. [https://doi.org/10.1002/\(sici\)1097-0363\(19970415\)24:7<645::aid-fld458>3.0.co;2-z](https://doi.org/10.1002/(sici)1097-0363(19970415)24:7<645::aid-fld458>3.0.co;2-z).
- Palisch, T.T., Vincent, M., Handren, P.J., 2010. Slickwater fracturing: food for thought. *SPE Prod. Oper.* 25, 327–344. <https://doi.org/10.2118/115766-PA>.
- Perkins, T.K., Kern, L.R., 1961. Widths of hydraulic fractures. *J. Pet. Technol.* 13, 937–949. <https://doi.org/10.2118/89-PA>.
- Pestana, J.M., Whittle, A.J., 1995. Compression model for cohesionless soils. *Geotechnique* 45, 611–631. <https://doi.org/10.1680/geot.1995.45.4.611>.
- Rahman, M.M., Rahman, M.K., 2010. A review of hydraulic fracture models and development of an improved Pseudo-3D model for stimulating tight oil/gas sand. *Energy Sources, Part A recover. Util. Environ. Eff.* 32, 1416–1436. <https://doi.org/10.1080/15567030903060523>.
- Shiozawa, S., McClure, M., 2016. Simulation of proppant transport with gravitational settling and fracture closure in a three-dimensional hydraulic fracturing simulator. *J. Pet. Sci. Eng.* 138, 298–314. <https://doi.org/10.1016/j.petrol.2016.01.002>.
- Sneddon, I.N., Elliott, H.A., 1946. The opening of a Griffith crack under internal pressure. *Quart. Appl. Math.* 4, 262–267.
- Stoddard, T., McLennan, J., Moore, J., Wagner, D., 2011. Fracture conductivity of a bauxite-propped geothermal system at in-situ conditions. In: *Thirty-sixth Workshop on Geothermal Reservoir Engineering*. Stanford University, Stanford.
- Tada, H., Paris, P.C., Irwin, G.R., 2000. Two-dimensional stress solutions for various configurations with cracks. In: *The Stress Analysis of Cracks Handbook*. ASME Press.
- Tinsley, J.M., Williams, J.R., 1975. A new method for providing increased fracture conductivity and improving stimulation results. *J. Pet. Technol.* 27, 1319–1325.
- van Dam, D.B., de Pater, C.J., Romijn, R., 2000. Analysis of hydraulic fracture closure in laboratory experiments. *SPE prod. Facil* 15, 151–158. <https://doi.org/10.2118/65066-PA>.
- Vincent, M.C., 2012. The next opportunity to improve hydraulic-fracture stimulation. *J. Pet. Technol.* 64, 118–127. <https://doi.org/10.2118/144702-JPT>.
- Wang, H.Y., Sharma, M.M., 2017. A non-local model for fracture closure on rough fracture faces and asperities. *J. Pet. Sci. Eng.* 154, 425–437. <https://doi.org/10.1016/j.petrol.2017.04.024>.
- Wang, J., Elsworth, D., 2017. Hydraulic fracturing with leakoff in a dual porosity medium. In: *51st US Rock Mechanics/Geomechanics Symposium*. American Rock Mechanics Association, San Francisco.
- Wang, J., Joseph, D.D., Patankar, N.A., Conway, M., Barree, R.D., 2003. Bi-power law correlations for sediment transport in pressure driven channel flows. *Int. J. Multiph. Flow* 29, 475–494. [https://doi.org/10.1016/S0301-9322\(02\)00152-0](https://doi.org/10.1016/S0301-9322(02)00152-0).
- Warpinski, N., 2010. Stress amplification and arch dimensions in proppant beds deposited by waterfracs. *SPE Prod. Oper.* 25, 1–17. <https://doi.org/10.2118/119350-PA>.
- Wen, Q., Zhang, S., Wang, L., Liu, Y., Li, X., 2007. The effect of proppant embedment upon the long-term conductivity of fractures. *J. Pet. Sci. Eng.* 55, 221–227. <https://doi.org/10.1016/j.petrol.2006.08.010>.
- Witherspoon, P.A., Wang, J.S.Y., Iwai, K., Gale, J.E., 1980. Validity of Cubic Law for fluid flow in a deformable rock fracture. *Water Resour. Res.* 16, 1016–1024. <https://doi.org/10.1029/WR016i006p01016>.
- Yan, X., Huang, Z., Yao, J., Song, W., Li, Y., Gong, L., 2016. Theoretical analysis of fracture conductivity created by the channel fracturing technique. *J. Nat. Gas. Sci.* Eng. 31, 320–330. <https://doi.org/10.1016/j.jngse.2016.03.038>.
- Zangerl, C., Evans, K.F., Eberhardt, E., Loew, S., 2008. Normal stiffness of fractures in granitic rock: a compilation of laboratory and in-situ experiments. *Int. J. Rock Mech. Min. Sci.* 45, 1500–1507. <https://doi.org/10.1016/j.ijrmms.2008.02.001>.
- Zheng, X., Chen, M., Hou, B., Ye, Z., Wang, W., Yin, C., Chen, X., 2017. Effect of proppant distribution pattern on fracture conductivity and permeability in channel fracturing. *J. Pet. Sci. Eng.* 149, 98–106. <https://doi.org/10.1016/j.petrol.2016.10.023>.
- Zimmerman, R.W., Bodvarsson, G.S., 1996. Hydraulic conductivity of rock fractures. *Transp. Porous Media* 23, 1–30. <https://doi.org/10.1007/BF00145263>.